CHEMISTRY OF MATERIALS

Open Access

pubs.acs.org/cm

Article

Effect of Metal *d* Band Position on Anion Redox in Alkali-Rich Sulfides

Published as part of Chemistry of Materials virtual special issue "C. N. R. Rao at 90".

Seong Shik Kim, David N. Agyeman-Budu, Joshua J. Zak, Jessica L. Andrews, Jonathan Li, Brent C. Melot, Johanna Nelson Weker, and Kimberly A. See*

Cite This: *Chem. Mater.* 2024, 36, 6454−6463

Read Online

ACCESS | Metrics & More | Article Recommendations | Supporting Information

ABSTRACT: New energy storage methods are emerging to increase the energy density of state-of-the-art battery systems beyond conventional intercalation electrode materials. For instance, employing anion redox can yield higher capacities compared with transition metal redox alone. Anion redox in sulfides has been recognized since the early days of rechargeable battery research. Here, we study the effect of *d*−*p* overlap in controlling anion redox by shifting the metal *d* band position relative to the S *p* band. We aim to determine the effect of shifting the *d* band position on the electronic structure and, ultimately, on charge compensation. Two isostructural sulfides $LiNaFeS_2$ and $LiNaCoS_2$ are directly compared to the hypothesis that the Co material should yield more covalent metal−anion bonds. $LiNaCoS_2$ exhibits a multielectron capacity of ≥1.7 electrons per formula unit, but despite the lowered Co *d* band, the voltage of anion redox is close to that of $LiNaFeS_2$. Interestingly, the material suffers from rapid capacity fade. Through a combination of solid-state nuclear magnetic resonance spectroscopy, Co and S X-ray absorption spectroscopy, X-ray diffraction, and partial density of states calculations, we demonstrate that oxidation of S nonbonding *p* states to S_2^{2-} occurs in early states of charge, which leads to an irreversible phase transition. We conclude that the lower energy of Co *d* bands increases their overlap with S *p* bands while maintaining S nonbonding *p* states at the same higher energy level, thus causing no alteration in the oxidation potential. Further, the higher crystal field stabilization energy for octahedral coordination over tetrahedral coordination is proposed to cause the irreversible phase transition in $LiNaCoS_2$.

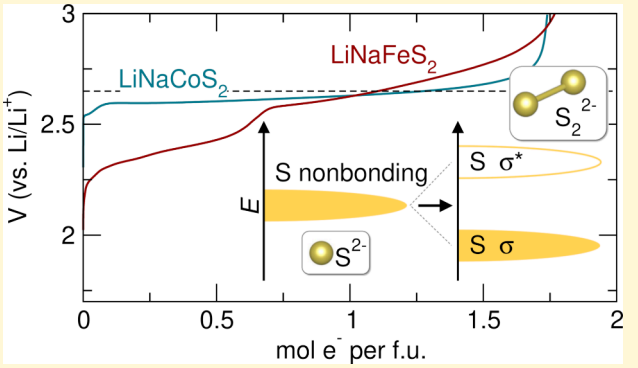

INTRODUCTION

Lithium-ion batteries (LIBs) have revolutionized the modern technological era, with applications ranging from powering portable electronic devices to electric vehicles.[1,2] Charge compensation of cathode materials in LIBs predominantly stems from the redox activity of *M d* states in $LiMO_2$, where *M* is a combination of transition metals that typically includes some combination of Al, Mn, Co, and Ni. From the original commercial intercalation-type oxide $LiCoO_2$, partial and/or full substitution of other metals such as Ni, Mn, and Al has enhanced the structural stability, increased the operating voltage energy density.[3−6]

To improve the energy density beyond the limits of conventional intercalation chemistry, there have been increasing efforts to leverage both cation and anion redox in the lattice to achieve multielectron storage.[7,8] We define multielectron redox as redox exceeding 1 mol of e^- per 1 mol of transition metal. While utilizing anion redox in so-called Li-rich oxides is highly desirable, many Li-rich oxide materials suffer from undesirable side reactions such as irreversible capacity loss, voltage fade, and electrolyte decomposition due to the unstable electronic configurations of oxidized structures.[8−12] The oxide literature is still grappling with conflicting mechanistic explanations for charge compensation in apparent multielectron materials.

An alternative approach to take advantage of anion redox is to replace the elemental O with the more covalent elemental S, at least with respect to the 3d transition metals, and develop Li-rich sulfide materials. Unlike metal oxides, metal sulfides have been known to form stable S_2^{2-} dimers without breaking the transition metal−S bond such as in TiS_3 ($Ti^{4+}S^{2-}(S_2)^{2-}$), pyrite ($M^{2+}(S_2)^{2-}$ where *M* = Mn, Fe, Co, Ni, Cu, Zn), or VS_4 ($V^{4+}(S_2)^{2-}$).[13−15] Data mining of the Inorganic Crystal

Received: February 22, 2024
Revised: June 9, 2024
Accepted: June 12, 2024
Published: June 21, 2024

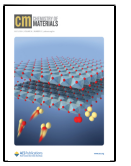

Structure Database (ICSD) has revealed that numerous thermodynamically stable binary and ternary moieties containing persulfide S_2^{2-} exist, highlighting the stable nature of S_2^{2-}.[12] Also, anion redox in Li-rich sulfides occurs within the electrochemical window of conventional carbonate electrolytes, making them excellent candidates to study anion redox and also as next-generation cathode materials. In fact, Li_2FeS_2, which is one of the first, if not the first Li-rich metal sulfide, can achieve energy densities of around 800 Wh/kg, despite the low operating voltage of 2.4 V because of the multielectron redox capabilities.

The Li-rich metal sulfides largely show the formation of persulfide bonds upon oxidation. However, the making and breaking of these bonds are likely a contributing factor to capacity fade and reduced rate performance compared to conventional intercalation. In this work, we aim to target a more covalent alkali-rich metal sulfide. We have a few hypotheses as to what could happen to anion oxidation with a more covalent metal−anion bond:

- More covalent metal−anion bonds will stabilize holes in the S band by distributing the charge over both the metal and the anion. Since holes are stabilized, the formation of persulfide bonds will be prevented, resulting in a more reversible and faster anion redox process.
- More covalent metal−anion bonds will shift the S *p* states down in energy due to hybridization/bonding with the metal *d* states resulting in a thermodynamic increase in the anion oxidation potential, which would increase energy density.
- More covalent metal−anion bonds will shift the hybridized states to lower energies without affecting the position of S nonbonding *p* states that may be revealed upon oxidation. If anion oxidation only occurs from the nonbonding states, then no shift in the oxidation potential would be observed.

A few examples already exist in which the relative positions of transition metal *d* states and S *p* states were tuned to study the nature of anion redox in Li-rich sulfide materials. Transition metal substitution of Fe^{2+}, Co^{2+}, and Ti^{3+} for Ti^{4+} in redox-inactive d^0 Li-rich Li_2TiS_3 has proven effective in activating S oxidation by introducing a redox-active transition metal whose *d* states overlap with those of S *p* states.[14,16−18] However, the oxidation mechanism is unclear from these studies. Additionally, greater *d*−*p* overlap can be achieved by shifting the *p* states. Substituting S with even more covalent Se ($Li_2FeS_{2-y}Se_y$, $Li_2TiS_{3-x}Se_x$, and $(Li_2Fe)S_{1-x}Se_xO$) has demonstrated that increasing transition metal−anion covalency through increasing Se content results in systematic decrease in the redox potential as a result of the formation of hybridized states of transition metal *d*, S *p*, and Se *p* bands.[19−21] As for comparing different redox-active transition metals in an isostructural phase, $(Li_2M)SO$ (M = Fe^{2+}, Mn^{2+}, and Co^{2+}) has been explored which revealed that although the role of S is not fully elucidated, partial substitution of Co improves the structural stability while that of Mn does not.[22−24]

In this work, we turn to alkali-rich sulfide $LiNaFeS_2$ that displays transition metal and $S^{2-}/(S_2)^{2-}$ redox couples and achieves reversible multielectron capacity.[25] From $LiNaFeS_2$, we substitute Co for Fe in an isostructural manner to form $LiNaCoS_2$. The Co *d* states are lower in energy and thus overlap more with S *p* states compared to $Fe^{2+/3+}$.[13,26] The shift of the *d* states is shown in a density of states (DOS) schematic in Figure 1. We hypothesize that the greater overlap of the metal *d* band with the anion *p* band will result in a more covalent metal−anion interaction, allowing us to determine how covalency might affect anion redox in two isostructural materials. We report that $LiNaCoS_2$ can be prepared via solid-state synthesis and is isostructural to previously reported Li_2FeS_2 and $LiNaFeS_2$.[25] $LiNaCoS_2$ exhibits multielectron capacity with anion redox in cycle 1, but the material is plagued by a rapid capacity fade from an irreversible conversion reaction that prevents further electrochemical activity. With a multitude of characterization techniques, including X-ray diffraction, solid-state nuclear magnetic resonance spectroscopy, and X-ray absorption spectroscopy, we report that S oxidation proceeds with S_2^{2-} formation and leads to the formation of thermodynamically stable pyrite CoS_2 and lithiated spinel phases.

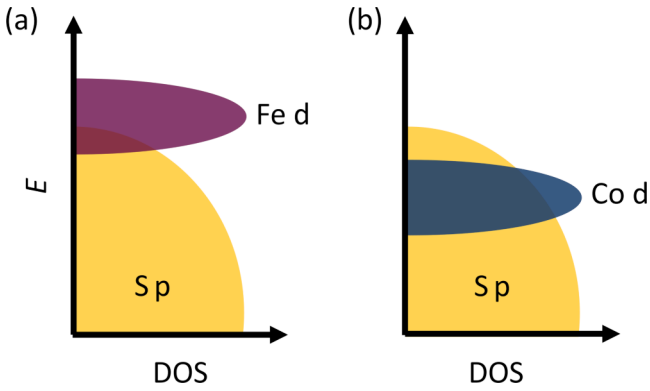

Figure 1. Schematic band structure showing the expected relative positions of isolated (a) Fe *d* band vs (b) the Co *d* band vs the S *p* band before bonding in $LiNaFeS_2$ and $LiNaCoS_2$.

EXPERIMENTAL SECTION

Material Preparation. All materials were stored and prepared in an Ar-filled glovebox in which the levels of O_2 and H_2O were below 1 ppm. $LiNaCoS_2$ was prepared using solid state methods, from Li_2S (Beantown Chemical, ≥99.9%), Na_2S (Fisher Scientific ≥99%), Co (Fisher Scientific, ≥99.8%), and S_8 (Acros Organics, ≥99.5%). Stoichiometric quantities of Li_2S, Na_2S, Co, and S_8 were ground, pressed into pellets of up to 400 mg, and sealed in a carbon-coated evacuated vitreous silica ampule. The sealed ampules were heated at 2 °C min^{-1} to 500 °C, dwelled for 96 h, and allowed to cool to room temperature in the furnace. The ampule was opened in a glovebox revealing a black pellet that was ground into powder. $LiNaCoS_2$ retains the pellet morphology upon completion of the reaction. The pristine $LiNaCoS_2$ pellet is dark gray/black, and the color is retained upon grinding.

Material Characterization. Powder X-ray diffraction (XRD) patterns were collected by using the Rigaku SmartLab diffractometer. The powders were placed on a 6 mm air-free sample holder (Rigaku) inside the glovebox to prevent air exposure. XRD patterns were collected with a Cu Kα X-ray source at 3° min^{-1} with 0.04° step size. The diffraction patterns were fit by the Rietveld method using GSAS-II.[27,28] Visualization of the crystal structures was aided by VESTA.[29]

High-resolution synchrotron powder X-ray diffraction (sXRD) patterns were collected at the Advanced Photon Source at Argonne National Laboratory on beamline 11-BM-B (λ = 0.4597 Å).[30] $LiNaCoS_2$ powder was used for the pristine state, while *ex situ* charged (fully polarized to 3 V) and discharged (fully charged to 3 V then discharged to 1.7 V) samples were prepared with 15 mg of a 60:20:20 wt % pellets of $LiNaCoS_2$, Super P carbon (TIMCAL), and PTFE.

https://doi.org/10.1021/acs.chemmater.4c00490
Chem. Mater. 2024, 36, 6454−6463

The cathode composite was recovered from the disassembled cell, washed with 200 μL of dimethyl carbonate, and vacuum-dried for more than 4 h. The sample was then sealed under vacuum in 0.7 mm (o.d.) glass capillaries (Hampton Research) to prevent air exposure and placed inside polyimide capillaries.

Operando XRD data were collected using a Bruker D8 Advance diffractometer in Bragg−Brentano geometry equipped with a Cu Kα source (λ_1 = 1.5406 Å, λ_2 = 1.5444 Å) and a Lynxeye XE-T detector. A custom-made *operando* cell with a PEEK body, stainless steel electrical contacts, and an X-ray-transparent Be window (SPI Supplies, 0.25 mm thick) was used. The Be window served as a current collector and allowed for X-ray penetration so that diffraction patterns could be collected while cycling galvanostatically. As with the *ex situ* cells, pellet electrodes composed of 60% active material, 20% carbon black, and 20% polymer binder were used and placed directly in the Be window. The pellet electrodes were cycled against Li foil using a BioLogic SP-200 potentiostat at a C/20 rate with one Whatman glass fiber separator (GF/D) flooded with 1 M $LiPF_6$ in a 1:1:3 EC:PC:DMC electrolyte. Patterns were continuously collected over a range of 10°−45° 2θ approximately every 20 min throughout the duration of the electrochemical cycling.

Solid-state nuclear magnetic resonance (ssNMR) spectroscopy was performed using a Bruker Avance 500 MHz spectrometer operating at 194.31 MHz for ^{7}Li and 132.29 MHz for ^{23}Na. All samples were packed in a 4 mm ZrO_2 HR-MAS rotor with a 50 μL PTFE spacer (Cortecnet). Pristine $LiNaCoS_2$ (30 mg) was packed into the rotor in an Ar-filled glovebox. *Ex situ* samples were prepared in the same way as electrochemical cells, with a total mass of 20 mg. ^{7}Li and ^{23}Na magic angle spinning (MAS) ssNMR was recorded at a spinning rate of 10.5 kHz. Single RF pulses of 0.5 μs−π/14 and 3 μs−π/2 were applied for ^{7}Li and ^{23}Na, respectively. A Bruker dual channel 4 mm wide variable temperature probe was used. Different spinning rates were used to identify the isotropic peaks. 1 M aqueous solutions of LiCl and NaCl were used as standards at 0 ppm. Not washing the composite electrode resulted in peaks from Li-containing impurities, such as the electrolyte salts.

Co and S K-edge X-ray absorption spectroscopy were conducted at beamline 4-3 at the Stanford Synchrotron Radiation Lightsource at SLAC National Accelerator Laboratory. Data processing including calibration and background correction was performed using Athena.[31] Co K-edge X-ray absorption spectroscopy data were calibrated to collinear Co foil for each sample. *Ex situ* samples were prepared in the same way as electrochemical cells with a total mass of 20 mg. All measurements were taken within 2 weeks of completing the electrochemical activity. Samples were transported in Ar-sealed pouches prepared in the glovebox to prevent exposure to air. *Ex situ* samples were placed onto the sample holder by using Kapton tape on each side inside an Ar-filled glovebox. During measurement, the sample holder was placed in a continuously He-flushed chamber with minimal O_2 concentration (<500 ppm). S K-edge XANES data were fit using the pseudo-Voigt function to highlight the emergence of a new peak.

Density functional theory (DFT) calculations were performed using SCAN parametrization with the Vienna *ab initio* Simulation Package (VASP). Interactions between core and valence electrons were accounted for with the projector augmented wave (PAW) pseudopotential method. The PAW pseudopotentials used treat the 1*s*, 2*s*, and 2*p* orbitals of Li (Li_{sv}); the 3*s* and 2*p* orbitals of Na (Na_{pv}); the 4*s* and 3*d* orbitals of Co; the 4*s* and 3*d* orbitals of Fe; and the 3*s* and 3*p* orbitals in S as valence states. The electronic structure was converged to a tolerance of 10^{-5} eV, using a Γ-centered reciprocal space discretization of 30K points per Å^{-1} along each reciprocal lattice vector and a plane-wave energy cutoff of 640 eV. All atomic positions were converged to a maximum force tolerance of 0.02 eV/Å. Static runs were performed on the relaxed structures using the tetrahedron method with Blochl corrections. Calculations were spin-polarized with magnetic moments initialized in both ferromagnetic and antiferromagnetic configurations. The antiferromagnetic configurations yield states with a lower energy by >50 meV/formula unit and are thus assumed to be the more stable configuration.

Crystal orbital Hamilton population (COHP) analysis was performed for the metal−S bond in the antiferromagnetic configurations using the LOBSTER package.[32−35] Interactions were calculated and summed for all nearest-neighbor metal−S bonds and normalized per formula unit. COHPs are plotted between the metal *d* and S *p* orbitals.

Electrochemical Characterization. All cells were prepared inside Ar-filled gloveboxes with H_2O and O_2 levels below 1 ppm. Powder of $LiNaCoS_2$ was mixed with Super P carbon (TIMCAL, ≥99%) and polytetrafluoroethylene (PTFE, Sigma-Aldrich) at 60:20:20 wt % to prepare free-standing composite electrodes. Approximately 10 mg of the composite mixture was pressed into 0.25 in. diameter pellets with a hand-operated arbor press (19.0 mg/cm^2 or 5.7 mAh/cm^2 based on 1.7 e$^-$ removal per formula unit). Coin cells (2032, MTI) were prepared with polished Li metal counter/reference electrodes, dried 18 mm diameter glass fiber separators (Whatman GF/D), and 11 drops of electrolyte (approximately 163 mg). A 1 M solution of $LiPF_6$ (Sigma-Aldrich, ≥99.99%) in a 1:1:3 mixture of ethylene carbonate (Sigma-Aldrich, >99%), propylene carbonate (Sigma-Aldrich, >99%), and dimethyl carbonate (Sigma-Aldrich, >99%) by volume was used as the electrolyte in all cells. Potentials reported here are in reference to the Li metal electrode potential, which is approximated to be equal to that of Li/Li$^+$. Galvanostatic cycling experiments were performed at C/10 based on 1 e$^-$ per formula unit. The galvanostatic intermittent titration technique (GITT) was conducted at a rate of C/10 based on 1 e$^-$ per formula unit for 20 min with 4 h open circuit hold rest periods.

RESULTS

DFT to Explore the Electronic Structure. A central hypothesis of this paper is that the covalency between the metal and the anion can be tuned by substituting Co for Fe in $LiNaFeS_2$. More covalent metal−anion bonds could help to stabilize holes in the S *p* band and/or lower the energy of the S *p* states and thermodynamically increase the anion oxidation potential, making sulfides a more viable cathode choice. By shifting from $LiNaFeS_2$ to $LiNaCoS_2$, we hypothesize that the lower energy *d* band of Co will overlap more with the S *p* band to yield a more covalent material. We first explore this hypothesis through DFT calculations of the electronic structure. The spin-polarized partial density of states (pDOS) for antiferromagnetic ordered forms of $LiNaFeS_2$ and $LiNaCoS_2$ is shown in Figure 2. Both materials exhibit a

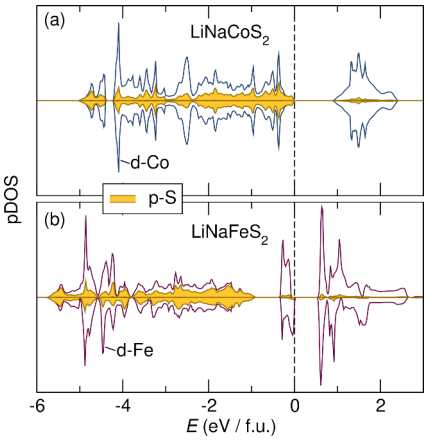

Figure 2. Calculated spin-polarized partial density of states of antiferromagnetic ordered forms of (a) $LiNaCoS_2$ and (b) $LiNaFeS_2$. A greater degree of Co−S overlap in $LiNaCoS_2$ is observed near the Fermi level compared to Fe−S overlap in $LiNaFeS_2$. $LiNaFeS_2$ shows significant Fe character near the Fermi level.

https://doi.org/10.1021/acs.chemmater.4c00490
Chem. Mater. 2024, 36, 6454−6463

small gap at the Fermi level, suggesting a semiconducting electronic ground state, though the band gap is an estimation as the calculations are conducted only with SCAN parametrizations. However, here we are more interested in the relative positions of the metal *d* states vs the S *p* states. The states below the Fermi level are composed of both S *p* and Co *d* character. The high degree of overlap suggests a more covalent Co−S bond compared to the Fe−S bond in $LiNaFeS_2$. $LiNaFeS_2$ shows a much higher degree of Fe character just below the Fermi level compared to S. To further evaluate the bonding character, the crystal orbital Hamilton population (COHP) analysis of the metal−S bonds in $LiNaCoS_2$ and $LiNaFeS_2$ is shown in the Supporting Information.

Structural Characterization. Although this paper focuses on the comparison between $LiNaFeS_2$ and $LiNaCoS_2$, we initially began our study targeting a comparison of Li_2FeS_2 and Li_2CoS_2—a simpler system with only one alkali element. Interestingly, using the same solid-state reaction conditions used for Li_2FeS_2 with Co substitution does not result in the formation of Li_2CoS_2, indicating that Li_2CoS_2 cannot be synthesized via traditional solid-state synthesis methods. However, alkali-rich $LiNaCoS_2$ can be prepared using similar reaction conditions to that of previously reported $LiNaFeS_2$.[25] Synchrotron X-ray diffraction (sXRD) is employed to characterize the structure of $LiNaCoS_2$. sXRD patterns and quantitative Rietveld refinement results of pristine $LiNaCoS_2$ are shown in Figure 3. $LiNaCoS_2$ adopts the $P\bar{3}m1$ space group

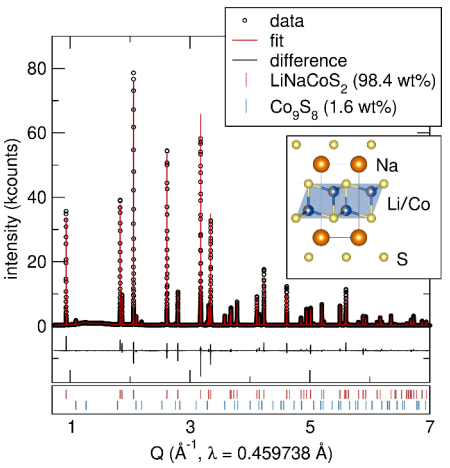

Figure 3. Synchrotron powder X-ray diffraction patterns and quantitative Rietveld refinement results of $LiNaCoS_2$. The $LiNaCoS_2$ unit cell is shown in the inset. The ticks indicate the Bragg reflection locations with a two-phase fit to 99.68% $LiNaCoS_2$ and 0.32% Co_9S_8.

and is isostructural to previously reported $LiNaFeS_2$.[25] In $LiNaCoS_2$, layers of edge-sharing Na octahedra are separated by layers of edge-sharing mixed Li/Co tetrahedra (Figure 3). The Li and Co are disordered and share the same tetrahedral site at a 1:1 ratio. The structure of $LiNaCoS_2$ was reported by Ren et al. and agrees with their assignment of the space group as well as mixed occupancy of Li and Co.[36] The sharp reflections indicate high crystallinity. The diffraction patterns are well-described by a two-phase fit to $LiNaCoS_2$ with a 0.0032 phase fraction of Co_9S_8 (<1.6 wt %), suggesting a very small impurity of Co_9S_8. The lattice parameters of $LiNaCoS_2$ are a = 3.95618 Å and c = 6.73845 Å and agree well with those reported by Ren et al., a = 3.95710 Å and c = 6.70108 Å.[36]

Electrochemical Characterization. To probe the effect of transition metal anion covalency on redox potential and reversibility, the electrochemical performance of $LiNaCoS_2$ is examined with galvanostatic cycling and compared to $LiNaFeS_2$. $LiNaFeS_2$ was first studied by Hansen et al.[25] Figure 4a depicts the first charge and discharge curve for both

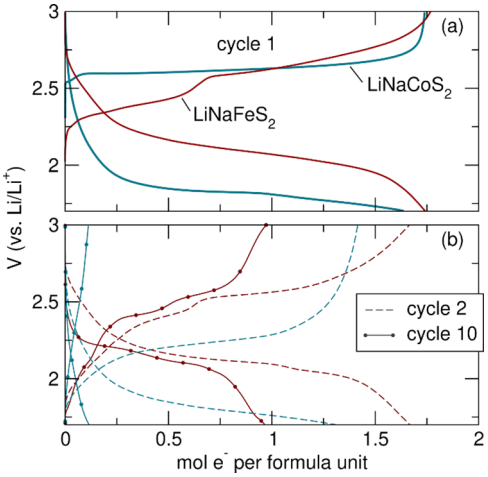

Figure 4. Galvanostatic cycling of $LiNaFeS_2$ compared with $LiNaCoS_2$ for (a) cycle 1 and (b) cycles 2 and 10. The materials are cycled at C/10 based on 1 e^- per formula unit.

materials at C/10 based on 1 e^- per formula unit (see Figure S1 for Q in mAh/g). The first charge of $LiNaFeS_2$ has been studied in detail previously.[25] Briefly, the first sloping region corresponds to Fe^{2+} oxidation to mixed $Fe^{2+/3+}$ followed by a kink and another sloping region corresponding to oxidation of S^{2-} to S_2^{2-}.[25] The average voltage of the anion oxidation region of the curve is 2.7 V. The capacity of $LiNaFeS_2$ reaches over 1.7 mol of e^- per formula unit.

Next, we discuss the first charge curve of $LiNaCoS_2$ and compare it with that of $LiNaFeS_2$. Perhaps unsurprisingly, the charge curve of $LiNaCoS_2$ bypasses the low voltage processes associated with Fe^{2+} oxidation in $LiNaFeS_2$. Instead, we observe a single plateau with an average potential of 2.6 V. Despite the presence of Co in the structure, the oxidation processes remain at very similar potentials compared to $LiNaFeS_2$. In fact, the voltage is comparable to potentials at which anion oxidation is suggested in other Li-rich sulfide materials.[14,17,18,20,25] Unlike the isostructural material $LiNaFeS_2$, no distinct region associated with transition metal oxidation is observed. This trend differs from anion-substituted $Li_2FeS_{2-y}Se_y$ in which mixing of the S and Se states yields a systematic shift in the voltage plateau.[19] The subsequent discharge cycle for $LiNaCoS_2$ is characterized mainly by a single plateau but at much lower potentials compared to the charge, resulting in large voltage hysteresis.

Next, we compare the cycling behavior of $LiNaFeS_2$ to that of $LiNaCoS_2$. The discharge and charge profiles for both materials are compared in Figure 4b. The capacity of $LiNaFeS_2$ fades somewhat quickly, largely due to particle fracturing associated with the removal of large Na^+.[37] Though the capacity fades, the cycle 1 and cycle 2 charge curves are similar in shape, suggesting that the mechanism is largely unchanged. $LiNaCoS_2$, however, shows much more rapid capacity fade losing most of its electrochemical activity by cycle 20 and displaying significant changes in shape as cycling continues.

https://doi.org/10.1021/acs.chemmater.4c00490
Chem. Mater. 2024, 36, 6454−6463

The capacity as a function of cycle number is shown in Supporting Information (Figure S2). The charge and discharge voltage profiles after cycle 1 resemble those of CoS_2 cycled between 3 and 1.6 V, suggesting a similar mechanism in $LiNaCoS_2$ after the first charge.[38] When charged to 3 V and then discharged to below 1 V, the discharge curve resembles that of CoS_2, further suggesting that charge products are similar to those of CoS_2 (Figure S3). The hysteresis remains high throughout the first cycle at around 0.5 V, which is much larger than that observed for $LiNaFeS_2$ (0.27 V at the start of anion oxidation, i.e., approximately 0.6 mol e^-[25]). The significant hysteresis coupled with the change in shape suggests that the oxidation mechanism is different in $LiNaCoS_2$ compared with $LiNaFeS_2$.

To probe overpotentials of $LiNaCoS_2$ during cycling and determine the origin of the hysteresis, the galvanostatic intermittent titration technique (GITT) is performed on $LiNaCoS_2$. The cell is polarized for 20 min at C/10 per formula unit with 4 h open circuit hold rest periods. The near-equilibrium potential at the end of each relaxation period is approximated as the equilibrium potential, V_{eq}, and the overpotential, η, represents the potential difference between the beginning and end of each rest period.

The GITT profiles for the first and second cycles of $LiNaCoS_2$ are plotted against the trace obtained at C/10 in Figure 5. The GITT profile during first charge reveals high

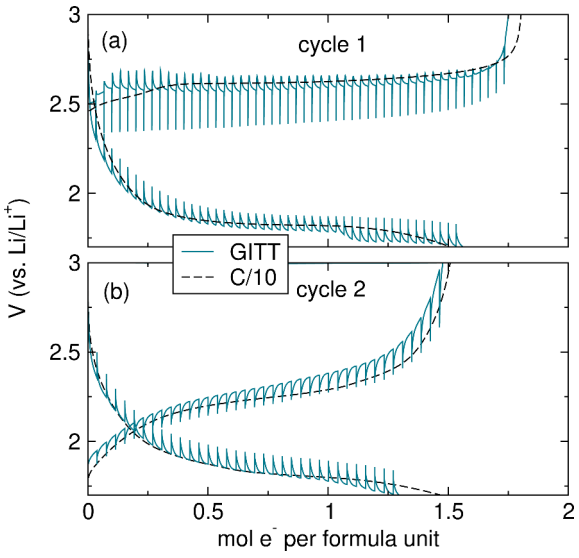

Figure 5. Near-equilibrium cycling curves of $LiNaCoS_2$ obtained by GITT compared with the galvanostatic cycling curves measured at C/10 for (a) cycle 1 and (b) cycle 2. GITT is measured at C/10 with 4 h rest periods every 20 m.

overpotentials. When the voltage profile is plotted as a function of time (Figure S4), the potential overshoots upon polarization suggesting nucleation and growth behavior.[39,40] When GITT is performed at C/100, the overpotential associated with the nucleation region decreases significantly (Figure S5), suggesting that the nucleation and growth behavior are caused by the sluggish kinetics. During discharge, an initial sloping region is followed by a plateau (Figure 5a). Also, the overpotential spike is no longer observed, and the overpotential is lower than during charge, suggesting an irreversible phase transition at the end of cycle 1. The large voltage hysteresis between charge and discharge equilibrium potentials further suggests that the charge and discharge pathways differ from each other.[41] In cycle 2, the charge and discharge GITT profiles trace the galvanostatic cycling data well and resemble that of CoS_2 cycled between 1.6 and 3 V, further suggesting irreversible phase transition.[38]

Structural and Spectroscopic Evolution during Cycling. Next, we undergo a series of studies to understand why $LiNaCoS_2$ cycles differently from $LiNaFeS_2$. First, we investigated the structural evolution of $LiNaCoS_2$ during cycling. Solid-state nuclear magnetic resonance (ssNMR) spectroscopy is employed to explore the local Li and Na environments. ^7Li and ^{23}Na magic-angle spinning (MAS) ssNMR spectra of $LiNaCoS_2$ at different states of charge collected at 10.5 kHz are shown in Figure 6. A single resonance

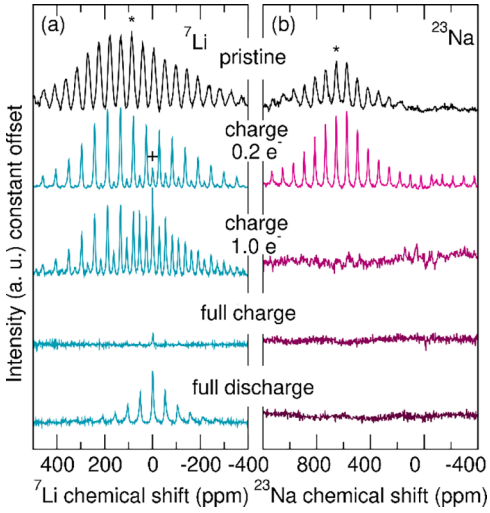

Figure 6. (a) ^7Li and (b) ^{23}Na MAS ssNMR spectra of $LiNaCoS_2$ in different states of charge. Pristine $LiNaCoS_2$ exhibits a single resonance marked ∗ in both ^7Li and ^{23}Na spectra, confirming a single environment for Li and Na. During charge, a new feature (+) is observed in ^7Li spectra while ^{23}Na spectra exhibit a decrease in intensity of the single resonance.

is observed at 87.4 and 652 ppm for ^7Li and ^{23}Na (marked ∗), respectively, indicating a single unique environment for both Li and Na in pristine $LiNaCoS_2$ and confirming the Wyckoff site assignments based on sXRD.

At 0.2 e^- charge (charge capacity equivalent to 0.2 e^- removal per formula unit), a new resonance is observed at −1 ppm in ^7Li MAS ssNMR (marked +), suggesting that a new Li environment begins to emerge at early states of charge. This new resonance grows in intensity during charge, as evidenced by the higher intensity in the spectrum of the material oxidized by 1.0 e^-, while the intensity of the original resonance at 87.4 ppm decreases. This result indicates that in addition to Li removal during charge, the active material undergoes a phase transition, resulting in a new Li environment. No new peaks are observed in the *operando* XRD (*vide infra*), so the new environment could be associated with small crystallites, an amorphous phase, or new Li environments associated with the structural distortions required for persulfide formation, for instance tetrahedral tilting.[25] At full charge (1.7 e^-), both resonances disappear in the ^7Li MAS ssNMR, suggesting that Li can be removed from the new environment. Meanwhile, ^{23}Na MAS ssNMR spectra reveal that the intensity of the single resonance in the pristine sample decreases throughout charge.

https://doi.org/10.1021/acs.chemmater.4c00490
Chem. Mater. 2024, 36, 6454−6463

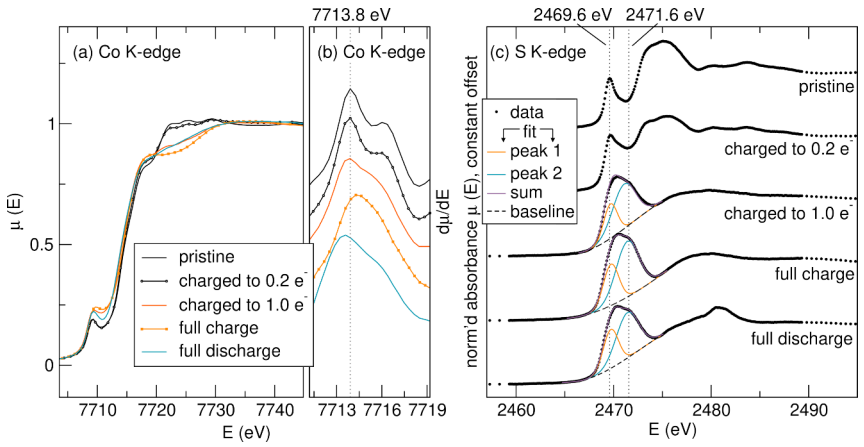

Figure 7. (a) Co K-edge XANES of $LiNaCoS_2$ at different states of charge and (b) the corresponding first-derivative plot of the rising edge. (c) S K-edge XANES of $LiNaCoS_2$ at the same states of charge. The pre-edge features in the S K-edge data are fit to pseudo-Voight functions to highlight the emergence of the new pre-edge feature at higher energies compared to the pre-edge feature of the pristine material. Co K-edge rising edge position does not shift in early states of charge and shifts at the end of charge, while S K-edge XANES reveals the emergence of a new pre-edge feature at early states of charge.

Na does not actively participate in the phase transition and is simply removed during charge. Additionally, ssNMR illustrates that intensities of both ^{7}Li and ^{23}Na resonances decrease during charge, indicating that both alkali ions are removed simultaneously and not in a discrete manner during charge. At the end of full charge, there are no visible resonances in both ^{7}Li and ^{23}Na ssNMR spectra although the charge capacity is 1.7 e^{-}. This may be due to the increasing paramagnetic influence from Co through oxidation that significantly broadens any residual resonances, making it difficult to quantify directly from the NMR measurements.

Upon full discharge, a single resonance is observed in the ^{7}Li spectrum while there are no resonances in the ^{23}Na spectrum, suggesting that only Li is incorporated during discharge. The resonance observed in the ^{7}Li spectrum appears at the same chemical shift as the one formed during charge, suggesting that the same lithiated structure is recovered. The original resonance at 87.4 ppm does not return, confirming that $LiNaCoS_2$ undergoes an irreversible phase transition on the first charge.

Next, we probed the structural evolution of $LiNaCoS_2$ with X-ray diffraction. *Operando* XRD patterns of $LiNaCoS_2$ reveal that reflections do not shift in position and lose intensity during charge, consistent with a two-phase mechanism (Figure S6). The low intensity of the peaks in the *operando* data makes it difficult to determine if any crystalline phases are formed during charge. We therefore turn to *ex situ* sXRD. sXRD patterns of fully charged and fully discharged $LiNaCoS_2$ are shown in Figure S7. The sXRD diffraction patterns exhibit low intensities compared to those of the pristine material shown in Figure 3. The sXRD patterns of both the fully charged and fully discharged $LiNaCoS_2$ can be fit to Co_9S_8 and CoS, with minor impurities that align with Li_2S reflections marked with an asterisk that are too low in intensity to be accurately fit. The phase fractions in both patterns are similar. Because both phases appear after charge and discharge, we suggest these phases are indicative of electrochemically inert phases that were already present in the pristine material. The charge product is therefore noncrystalline and may be either solid or dissolved in the electrolyte. Interestingly, there are no visible signs of polysulfide dissolution upon disassembly of the cell, and ultraviolet−visible (UV−vis) spectroscopy shows no evidence of polysulfide dissolution in the electrolyte (Figure S8).

Additionally, we note that while ssNMR results indicate that the alkali metal ion in the discharge product is predominantly Li (Figure 6), the intensity of the Li_2S peaks do not change significantly, and we do not observe any Li-containing crystalline phase in the sXRD. The same trend is observed by Butala et al., who reported that the weighting of Li_2S does not increase upon deep discharge in Li−CoS_2 below 1.6 V.[42] The Li could be incorporated in small domains of Li_2S that do not result in an increase in the Li_2S reflection intensities or incorporated into the cathode through a different pathway. The lower voltage cutoff of 1.7 V suggests that Li_2S is likely not formed.[38,42] Also, ^{7}Li MAS ssNMR indicates that the Li environment in full discharge resembles the one that forms during charge, further suggesting a lithiated phase other than Li_2S such as $Li_xCo_3S_4$ or $Li_xCo_9S_8$. S K-edge X-ray absorption spectroscopy data also suggest that Li_2S does not form (*vide infra*).

Next, the oxidation state and local environment of Co and S are probed with X-ray absorption spectroscopy (XAS) to gain insight into the charge compensation mechanism. Figure 7 shows the *ex situ* Co and S K-edge X-ray absorption near-edge structure (XANES) of $LiNaCoS_2$ at various states of charge. A pre-edge feature associated with the 1*s* to 3*d* transition is observed in the pristine $LiNaCoS_2$ in Co K-edge XANES, confirming the presence of tetrahedrally coordinated Co (Figure 7a).[42−44] The position of the rising edge, which gives an indication of the oxidation state of Co, is more easily observed by plotting the first derivative of the XAS spectrum, as shown in Figure 7b. Upon full charge, the edge shifts to higher energy, suggesting Co oxidation (Figure 7b). Quantitative determination of the edge shift is difficult to determine due to the overlap between the edge and the pre-edge features. Upon full discharge, the rising edge shifts to a lower energy than that measured in the pristine material, and the overall shape of the Co K-edge XANES region is not reversible at the end of cycle 1, suggesting Co reduction and an irreversible phase transition.

To probe the activity of S in the charge compensation mechanism, we also measured the S K-edge XANES. The S K-

https://doi.org/10.1021/acs.chemmater.4c00490
Chem. Mater. 2024, 36, 6454−6463

edge XANES at various states of charge is shown in Figure 7c. The S K-edge spectrum of pristine $LiNaCoS_2$ exhibits a similar shape compared with the isostructural material $LiNaFeS_2$ with an intense pre-edge feature at 2469.6 eV (Figure S9). The pre-edge feature is associated with the S 1*s* to Co 3*d* transition and is intense due to the covalent nature of the Co−S bond.[25,45] Upon charge, a new feature emerges at a higher energy, suggesting a new transition associated with more oxidized S relative to S^{2-}. We fit the pre-edge region with pseudo-Voight functions to highlight the emergence of this new feature. The fits suggest the new feature is centered at 2471.6 eV, and it grows in intensity during charge. A similar feature is observed when $LiNaFeS_2$ is charged and it has been associated with the formation of persulfide bonds due to sulfide oxidation.[25] In $LiNaFeS_2$ the higher energy pre-edge feature disappears upon discharge. The discharged S K-edge XANES of $LiNaCoS_2$, however, still shows the new feature at 2471.6 eV, suggesting that upon reduction oxidized S still remains. This will be discussed further in the next section.

Discussion. The comparison between the electrochemical behavior of $LiNaCoS_2$ vs $LiNaFeS_2$ can provide important insights into the battle between conversion and reversible anion redox in materials whose anionic *p* bands can be electrochemically accessed. First, we discuss the behavior of $LiNaCoS_2$ and then compare it to $LiNaFeS_2$. Electrochemical and structural characterization techniques indicate a conversion reaction when charging $LiNaCoS_2$. GITT experiments show nucleation behavior upon polarization, suggesting the formation of a new phase upon charge. In addition to the relatively large kinetic overpotentials observed in the GITT, which is reminiscent of kinetic overpotentials for other S-based anion redox materials, the conversion mechanism also results in significant thermodynamic hysteresis on cycle 1. Interestingly, despite the conversion mechanism, the oxidation does not involve the formation of polysulfide, S_x^{2-}, intermediates, or products since no visible discoloration of the separator after cycling is observed and UV−vis of the electrolyte shows no new spectral features after charging. ^{7}Li MAS ssNMR reveals a new resonance at early states of charge, confirming the presence of a new phase containing Li. Such behavior is very different from the electrochemistry of $LiNaFeS_2$, though both materials can be oxidized to roughly the same state of charge, both yielding a capacity of around 1.7 e^- per formula unit. The hysteresis observed for $LiNaFeS_2$ is much lower, and though the material shows capacity fade largely due to the removal of the large Na^+,[37] the shape of the second charge curve is similar to the first. Therefore, while $LiNaCoS_2$ undergoes conversion on cycle 1 to yield a material dissimilar to the parent phase, $LiNaFeS_2$ does not.

Though polysulfides are not observed, the large capacity of $LiNaFeS_2$ suggests contributions from the anions. S K-edge XANES provides insights into the charge compensation mechanism upon charging of $LiNaCoS_2$. A new pre-edge feature at higher energy in addition to a shift in the edge position is observed upon charging. Both changes in the S K-edge indicate the presence of oxidized S^{2-}. The new pre-edge feature coincides with the pre-edge feature measured in pyrite CoS_2, which is composed solely of persulfides, S_2^{2-}.[46] The new pre-edge feature appears at early states of charge and does not increase significantly upon full charge. Meanwhile, the Co rising edge does not shift until charging >1.0 e^- and shifts to a higher energy upon full charge. This result corroborates the pDOS calculations that S^{2-} oxidation accounts for most of the charge compensation, initially followed by Co oxidation during charge. Based on the pDOS calculations and Co and S K-edge XANES, we propose that S is oxidized initially which forces a phase transition to a phase that contains persulfides. Co-containing persulfides are known to be thermodynamically stable materials, like CoS_2. A discussion surrounding the possible phases formed during $LiNaCoS_2$ oxidation can be found in the Supporting Information.

Crystal field theory provides useful insights into the stability of $LiNaMS_2$ (*M* = Co or Fe) with tetrahedrally coordinated *M*. In $LiNaCoS_2$, the electron configuration of Co^{2+} is d^7, which favors octahedral coordination over tetrahedral due to the higher crystal field stabilization energy (CFSE) of 0.27 Δ_o. Because Co *d* states are buried underneath the S *nb* states, the formal oxidation state of Co remains as 2+ in the initial states of charge during which alkali metal ions are removed and S^{2-} is oxidized. Subsequently, $LiNaCoS_2$ is no longer in its initial metastable phase, and we hypothesize that CFSE acts as the driving force for Co to convert to CoS_2 in which Co^{2+} is in an octahedral environment and also oxidized S forms S_2^{2-}. Additionally, ternary Li_2CoS_2 does not form in the same solid-state reaction conditions used to synthesize Li_2FeS_2, suggesting that larger Na ions stabilize the structure and enable the formation of $LiNaCoS_2$, and the removal of Na ions disrupts the stability of the pristine phase. In short, the lower energies of metal *d* states reveal S nonbonding *p* states for oxidation. As S nonbonding *p* states are oxidized, persulfide bonds form. This process is marked by significant structural distortion, including persulfide formation and alkali removal, which perturbs the metastable, tetrahedrally coordinated d^7 Co^{2+} with a higher CFSE and forces Co into an octahedral environment.

In contrast, the electron configuration of Fe^{2+} in $LiNaFeS_2$ is d^6 for which the CFSE, 0.13 Δ_o, is smaller than d^7 Co^{2+}. Additionally, $Fe^{2+/3+}$ oxidation occurs first in $LiNaFeS_2$, yielding 0.5 e^- removal per formula unit due to the higher Fe *d* states compared to Co *d* states. Subsequent shifting of the electron configuration from Fe^{2+} d^6 to Fe^{3+} d^5 in the process results in 0 Δ_o and no propensity for either octahedral or tetrahedral coordination over the other. As a result, $LiNaFeS_2$ does not undergo phase transition, and the tetrahedral Fe environment remains throughout cycling. Lastly, we note that partial substitution of Co for Fe in $LiNaFeS_2$ does not improve the electrochemical performance of the material (Figures S10 and S11).

What is additionally interesting to note is the voltage of the charge curves for $LiNaCoS_2$ vs $LiNaFeS_2$. If the initial sloping region in $LiNaFeS_2$ associated with Fe^{2+} is ignored, then the oxidation potential of both $LiNaCoS_2$ and $LiNaFeS_2$ is largely the same. Both materials undergo anion oxidation in this potential region, and the fact that the voltage does not shift suggests that the position of the metal *d* band does not affect the S^{2-} oxidation. We therefore suggest that anion oxidation in sulfides is occurring from a nonbonding *p* band, shown schematically in Figure 8, and thus, tuning the potential of anion oxidation cannot be achieved through modulating covalency. Said another way, anion oxidation cannot be thermodynamically stabilized by incorporating more metal character into the *p* band.

CONCLUSIONS

$LiNaCoS_2$ that is isostructural to $LiNaFeS_2$ can be synthesized, allowing for a direct comparison between a Co-containing

https://doi.org/10.1021/acs.chemmater.4c00490
Chem. Mater. 2024, 36, 6454−6463

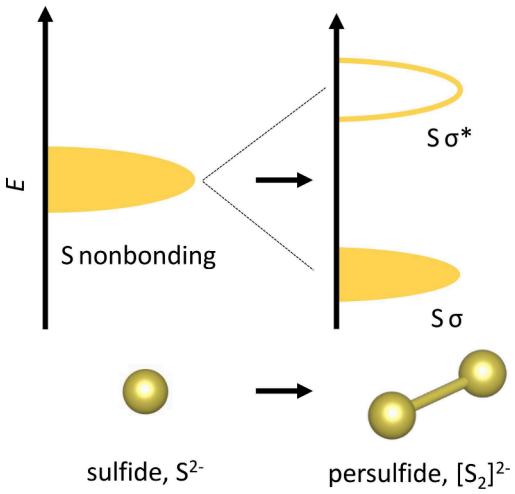

Figure 8. Schematic DOS cartoon showing oxidation of S occurs from S nonbonding bands, leading to a new σ and σ^* band associated with the rehybridization of the S p band and the formation of S−S bonds.

alkali-rich metal sulfide and an Fe-containing alkali-rich metal sulfide. The Co d band lies significantly deeper in the S p band compared to Fe, allowing us to determine how the metal d band position affects anion redox. We find that $LiNaCoS_2$ exhibits multielectron capacity from both cation and anion redox, similar to that of $LiNaFeS_2$.

However, unlike $LiNaFeS_2$ which shows Fe^{2+} oxidation followed by S^{2-} oxidation, $LiNaCoS_2$ undergoes S^{2-} oxidation first followed by Co^{2+} oxidation during charge. Also, despite the change in metal identity, the voltage of anion oxidation occurs at the same potential in both the Co- and Fe-containing materials. We conclude that despite the increased overlap between anion p band and metal d band, the S nonbonding p states remain at the same energy level, and consequently, the oxidation potential does not shift. Thus, metal−anion mixing cannot be used to tune the anion oxidation potential in Li-rich sulfides. Lastly, unlike $LiNaFeS_2$, $LiNaCoS_2$ undergoes an irreversible phase transition in cycle 1 that we hypothesize is driven by crystal field stabilization energy of Co^{2+}.

■ ASSOCIATED CONTENT

Supporting Information

The Supporting Information is available free of charge at https://pubs.acs.org/doi/10.1021/acs.chemmater.4c00490.

First cycle capacity in mAh/g, capacity as a function of cycle number, galvanostatic cycling data of charged to 3 V then discharged to 1 V, galvanostatic intermittent titration technique of $LiNaCoS_2$, galvanostatic intermittent titration technique at C/100, *operando* XRD patterns of $LiNaCoS_2$, synchrotron XRD patterns at full charge and full discharge, UV−vis spectra of control and charged $LiNaCoS_2$, S K-edge XANES data comparison of $LiNaFeS_2$ and $LiNaCoS_2$, ^{7}Li MAS ssNMR spectra of $LiNaCoS_2$ and $Li_6Co_9S_8$, XRD patterns of $LiNaCo_xFe_{1-x}S_2$, galvanostatic cycling data of $LiNaCo_xFe_{1-x}S_2$, discussion of possible phases formed during oxidation of $LiNaCoS_2$ (PDF)

■ AUTHOR INFORMATION

Corresponding Author

Kimberly A. See − *Division of Chemistry and Chemical Engineering, California Institute of Technology, Pasadena, California 91125, United States;* orcid.org/0000-0002-0133-9693; Email: ksee@caltech.edu

Authors

Seong Shik Kim − *Division of Chemistry and Chemical Engineering, California Institute of Technology, Pasadena, California 91125, United States;* orcid.org/0000-0003-2604-6392

David N. Agyeman-Budu − *Stanford Synchrotron Radiation Lightsource, SLAC National Accelerator Laboratory, Menlo Park, California 94025, United States*

Joshua J. Zak − *Division of Chemistry and Chemical Engineering, California Institute of Technology, Pasadena, California 91125, United States;* orcid.org/0000-0003-3793-7254

Jessica L. Andrews − *Department of Chemistry, University of Southern California, Los Angeles, California 90089, United States*

Jonathan Li − *Materials Department, University of California, Santa Barbara, Santa Barbara, California 93106, United States;* orcid.org/0000-0003-2632-0080

Brent C. Melot − *Department of Chemistry, University of Southern California, Los Angeles, California 90089, United States; Department of Chemical Engineering and Materials Science, University of Southern California, Los Angeles, California 90089, United States;* orcid.org/0000-0002-7078-8206

Johanna Nelson Weker − *Stanford Synchrotron Radiation Lightsource, SLAC National Accelerator Laboratory, Menlo Park, California 94025, United States;* orcid.org/0000-0001-6856-3203

Complete contact information is available at: https://pubs.acs.org/10.1021/acs.chemmater.4c00490

Notes

The authors declare no competing financial interest.

■ ACKNOWLEDGMENTS

This work was supported by the Center for Synthetic Control Across Length-scales for Advancing Rechargeables (SCALAR), an Energy Frontier Research Center funded by the U.S. Department of Energy, Office of Science, Basic Energy Sciences, under Award No. DE-SC0019381. Use of the Stanford Synchrotron Radiation Lightsource, SLAC National Accelerator Laboratory, is supported by the U.S. Department of Energy, Office of Science, Office of Basic Energy Sciences under Contract No. DE-AC02-76SF00515. Use of the Advanced Photon Source at Argonne National Laboratory was supported by the U.S. Department of Energy, Office of Science, Office of Basic Energy Sciences, under Contract No. DE-AC02-06CH11357. Computational facilities were used that were purchased with funds from the National Science Foundation (CNS-1725797) and administered by the Center for Scientific Computing (CSC). The CSC is supported by the California NanoSystems Institute and the Materials Research Science and Engineering Center (MRSEC; NSF DMR 2308708) at UC Santa Barbara. K.A.S. acknowledges support from the David and Lucile Packard Foundation, Alfred P.

Sloan Foundation, and Camille and Henry Dreyfus Foundation. J.L.A. acknowledges support from the National Science Foundation Graduate Research Fellowship Program under Grant No. DGE-1842487. The authors thank Dr. Sonjong Hwang for technical assistance and helpful discussions regarding the solid-state NMR and Prof. Anton Van der Ven for helpful discussions.

REFERENCES

(1) Zeng, X.; Li, M.; Abd El-Hady, D.; Alshitari, W.; Al-Bogami, A. S.; Lu, J.; Amine, K. Commercialization of Lithium Battery Technologies for Electric Vehicles. *Adv. Energy Mater.* **2019**, *9*, 1900161.

(2) Fichtner, M. Recent Research and Progress in Batteries for Electric Vehicles. *Batteries & Supercaps* **2022**, *5*, e202100224.

(3) Amatucci, G. G.; Tarascon, J. M.; Klein, L. C. CoO_2, The End Member of the $LiCoO_2$ Solid Solution. *J. Electrochem. Soc.* **1996**, *143*, 1114−1123.

(4) Blomgren, G. E. The Development and Future of Lithium Ion Batteries. *J. Electrochem. Soc.* **2017**, *164*, A5019−A5025.

(5) Märker, K.; Reeves, P. J.; Xu, C.; Griffith, K. J.; Grey, C. P. Evolution of Structure and Lithium Dynamics in $LiNi_{0.8}Mn_{0.1}Co_{0.1}O_2$ (NMC811) Cathodes during Electrochemical Cycling. *Chem. Mater.* **2019**, *31*, 2545−2554.

(6) Chakraborty, A.; Kunnikuruvan, S.; Kumar, S.; Markovsky, B.; Aurbach, D.; Dixit, M.; Major, D. T. Layered Cathode Materials for Lithium-Ion Batteries: Review of Computational Studies on $LiNi_{1-x-y}Co_xMn_yO_2$ and $LiNi_{1-x-y}Co_xAl_yO_2$. *Chem. Mater.* **2020**, *32*, 915−952.

(7) Radin, M. D.; Hy, S.; Sina, M.; Fang, C.; Liu, H.; Vinckeviciute, J.; Zhang, M.; Whittingham, M. S.; Meng, Y. S.; Van der Ven, A. Narrowing the Gap between Theoretical and Practical Capacities in Li-Ion Layered Oxide Cathode Materials. *Adv. Energy Mater.* **2017**, *7*, 1602888.

(8) Assat, G.; Tarascon, J.-M. Fundamental Understanding and Practical Challenges of Anionic Redox Activity in Li-ion Batteries. *Nature Energy* **2018**, 1.

(9) Renfrew, S. E.; McCloskey, B. D. Residual Lithium Carbonate Predominantly Accounts for First Cycle CO_2 and CO Outgassing of Li-Stoichiometric and Li-Rich Layered Transition-Metal Oxides. *J. Am. Chem. Soc.* **2017**, *139*, 17853−17860.

(10) Kaufman, L. A.; McCloskey, B. D. Surface Lithium Carbonate Influences Electrolyte Degradation via Reactive Oxygen Attack in Lithium-Excess Cathode Materials. *Chem. Mater.* **2021**, *33*, 4170−4176.

(11) Rana, J.; Papp, J. K.; Lebens-Higgins, Z.; Zuba, M.; Kaufman, L. A.; Goel, A.; Schmuch, R.; Winter, M.; Whittingham, M. S.; Yang, W.; McCloskey, B. D.; Piper, L. F. J. Quantifying the Capacity Contributions during Activation of Li_2MnO_3. *ACS Energy Lett.* **2020**, *5*, 634−641.

(12) Zak, J. J.; Kim, S. S.; Laskowski, F. A. L.; See, K. A. An Exploration of Sulfur Redox in Lithium Battery Cathodes. *J. Am. Chem. Soc.* **2022**, *144*, 10119−10132.

(13) Rouxel, J. Anion- Cation Redox Competition and the Formation of New Compounds in Highly Covalent Systems. *Chem.—Eur. J.* **1996**, *2*, 1053−1059.

(14) Saha, S.; Assat, G.; Sougrati, M. T.; Foix, D.; Li, H.; Vergnet, J.; Turi, S.; Ha, Y.; Yang, W.; Cabana, J.; Rousse, G.; Abakumov, A. M.; Tarascon, J.-M. Exploring the Bottlenecks of Anionic Redox in Li-rich Layered Sulfides. *Nat. Energy* **2019**, *4*, 977−987.

(15) Kitchaev, D. A.; Vinckeviciute, J.; Van der Ven, A. Delocalized Metal−Oxygen π-Redox Is the Origin of Anomalous Nonhysteretic Capacity in Li-Ion and Na-Ion Cathode Materials. *J. Am. Chem. Soc.* **2021**, *143*, 1908−1916.

(16) Flamary-Mespoulie, F.; Boulineau, A.; Martinez, H.; Suchomel, M. R.; Delmas, C.; Pecquenard, B.; Le Cras, F. Lithium-Rich Layered Titanium Sulfides: Cobalt- and Nickel-free High Capacity Cathode Materials for Lithium-Ion Batteries. *Energy Storage Materials* **2020**, *26*, 213−222.

(17) Li, B.; Jiang, N.; Huang, W.; Yan, H.; Zuo, Y.; Xia, D. Studies on Anionic Redox in Li-Rich Cathode Materials of Li-Ion Batteries. *Springer Singapore* **2019**, 99−121.

(18) Nagarajan, S.; Hwang, S.; Balasubramanian, M.; Thangavel, N. K.; Arava, L. M. R. Mixed Cationic and Anionic Redox in Ni and Co Free Chalcogen-Based Cathode Chemistry for Li-Ion Batteries. *J. Am. Chem. Soc.* **2021**, *143* (38), 15732−15744.

(19) Martinolich, A. J.; et al. Controlling Covalency and Anion Redox Potentials through Anion Substitution in Li-Rich Chalcogenides. *Chem. Mater.* **2021**, *33*, 378−391.

(20) Leube, B. T.; Robert, C.; Foix, D.; Porcheron, B.; Dedryvère, R.; Rousse, G.; Salager, E.; Cabelguen, P.-E.; Abakumov, A. M.; Vezin, H.; Doublet, M.-L.; Tarascon, J.-M. Activation of Anionic Redox in D0 Transition Metal Chalcogenides by Anion Doping. *Nat. Commun.* **2021**, *12*, 5485.

(21) Mohamed, M. A. A.; Gorbunov, M. V.; Valldor, M.; Hampel, S.; Gräßler, N.; Mikhailova, D. Tuning the Electrochemical Properties by Anionic Substitution of Li-rich Antiperovskite $(Li_2Fe)S_{1-x}Se_xO$ Cathodes for Li-ion Batteries. *J. Mater. Chem. A* **2021**, *9*, 23095−23105.

(22) Lai, K. T.; Antonyshyn, I.; Prots, Y.; Valldor, M. Anti-Perovskite Li-Battery Cathode Materials. *J. Am. Chem. Soc.* **2017**, *139*, 9645−9649.

(23) Mikhailova, D.; Giebeler, L.; Maletti, S.; Oswald, S.; Sarapulova, A.; Indris, S.; Hu, Z.; Bednarcik, J.; Valldor, M. Operando Studies of Antiperovskite Lithium Battery Cathode Material $(Li_2Fe)SO$. *ACS Appl. Energy Mater.* **2018**, *1*, 6593−6599.

(24) Gorbunov, M. V.; Carocci, S.; Gonzalez Martinez, I. G.; Baran, V.; Mikhailova, D. Studies of $Li_2Fe_{0.9}M_{0.1}SO$ Antiperovskite Materials for Lithium−Ion Batteries: The Role of Partial Fe^{2+} to M^{2+} Substitution. *Front. Energy Res.* **2021**, *9*, 657962.

(25) Hansen, C. J.; Zak, J. J.; Martinolich, A. J.; Ko, J. S.; Bashian, N. H.; Kaboudvand, F.; Van der Ven, A.; Melot, B. C.; Nelson Weker, J.; See, K. A. Multielectron, Cation and Anion Redox in Lithium-Rich Iron Sulfide Cathodes. *J. Am. Chem. Soc.* **2020**, *142*, 6737−6749.

(26) Kim, Y.; Goodenough, J. B. Lithium Insertion into Transition-Metal Monosulfides: Tuning the Position of the Metal 4s Band. *J. Phys. Chem. C* **2008**, *112*, 15060−15064.

(27) McCusker, L. B.; Von Dreele, R. B.; Cox, D. E.; Louer, D.; Scardi, P. Rietveld Refinement Guidelines. *J. Appl. Crystallogr.* **1999**, *32*, 36−50.

(28) Toby, B. H.; Von Dreele, R. B. GSAS-II: The Genesis of a Modern Open-Source All Purpose Crystallography Software Package. *J. Appl. Crystallogr.* **2013**, *46*, 544−549.

(29) Momma, K.; Izumi, F. VESTA 3 for Three-Dimensional Visualization of Crystal, Volumetric and Morphology Data. *J. Appl. Crystallogr.* **2011**, *44*, 1272−1276.

(30) Wang, J.; Toby, B. H.; Lee, P. L.; Ribaud, L.; Antao, S. M.; Kurtz, C.; Ramanathan, M.; Von Dreele, R. B.; Beno, M. A. A Dedicated Powder Diffraction Beamline at the Advanced Photon Source: Commissioning and Early Operational Results. *Rev. Sci. Instrum.* **2008**, *79*, 085105.

(31) Ravel, B.; Newville, M. ATHENA, ARTEMIS, HEPHAESTUS: Data Analysis for X-ray Absorption Spectroscopy Using IFEFFIT. *J. Synchrotron Rad* **2005**, *12*, 537−541.

(32) Dronskowski, R.; Bloechl, P. E. Crystal orbital Hamilton populations (COHP): energy-resolved visualization of chemical bonding in solids based on density-functional calculations. *J. Phys. Chem.* **1993**, *97*, 8617−8624.

(33) Deringer, V. L.; Tchougréeff, A. L.; Dronskowski, R. Crystal orbital Hamilton population (COHP) analysis as projected from plane-wave basis sets. *J. Phys. Chem. A* **2011**, *115*, 5461−5466.

(34) Maintz, S.; Deringer, V. L.; Tchougréeff, A. L.; Dronskowski, R. Analytic projection from plane-wave and PAW wavefunctions and application to chemical-bonding analysis in solids. *Journal of computational chemistry* **2013**, *34*, 2557−2567.

https://doi.org/10.1021/acs.chemmater.4c00490
Chem. Mater. 2024, 36, 6454−6463

(35) Maintz, S.; Deringer, V. L.; Tchougréeff, A. L.; Dronskowski, R. LOBSTER: A tool to extract chemical bonding from plane-wave based DFT, 2016.
(36) Ren, Y.; Lai, X.; Guo, M.; Wang, R.; Deng, J.; Jian, J. Synthesis, Structure and Physical Properties of Layered Quaternary Sulfides $NaLiMS_2$ (M = Mn, Fe, Co). *J. Alloys Compd.* **2020**, *822*, 153613.
(37) Kim, S. S.; Agyeman-Budu, D. N.; Zak, J. J.; Dawson, A.; Yan, Q.; Cában-Acevedo, M.; Wiaderek, K. M.; Yakovenko, A. A.; Yao, Y.; Irshad, A.; Narayan, S. R.; Luo, J.; Nelson Weker, J.; Tolbert, S. H.; See, K. A. Promoting Reversibility of Multielectron Redox in Alkali-Rich Sulfide Cathodes through Cryomilling. *Chem. Mater.* **2022**, *34*, 3236−3245.
(38) Yan, J.; Huang, H.; Zhang, J.; Liu, Z.; Yang, Y. A Study of Novel Anode Material CoS_2 for Lithium Ion Battery. *J. Power Sources* **2005**, *146*, 264−269.
(39) Pei, A.; Zheng, G.; Shi, F.; Li, Y.; Cui, Y. Nanoscale Nucleation and Growth of Electrodeposited Lithium Metal. *Nano Lett.* **2017**, *17*, 1132−1139.
(40) Mohammadi, A.; Monconduit, L.; Stievano, L.; Younesi, R. Measuring the Nucleation Overpotential in Lithium Metal Batteries: Never Forget the Counter Electrode! *J. Electrochem. Soc.* **2022**, *169*, 070509.
(41) Van der Ven, A.; See, K. A.; Pilon, L. Hysteresis in Electrochemical Systems. *Battery Energy* **2022**, *1*, 20210017.
(42) Butala, M. M.; Doan-Nguyen, V. V. T.; Lehner, A. J.; Göbel, C.; Lumley, M. A.; Arnon, S.; Wiaderek, K. M.; Borkiewicz, O. J.; Chapman, K. W.; Chupas, P. J.; Balasubramanian, M.; Seshadri, R. Operando Studies Reveal Structural Evolution with Electrochemical Cycling in Li-CoS_2. *J. Phys. Chem. C* **2018**, *122*, 24559−24569.
(43) Bouwens, S. M. A. M.; Koningsberger, D. C.; de Beer, V. H. J.; Prins, R. The Structure of the Cobalt Sulfide Phase in Carbon-supported Co and Co-Mo Sulfide Catalysts as Studied by EXAFS and XANES. *Catal. Lett.* **1988**, *1*, 55−59.
(44) Shulman, G. R.; Yafet, Y.; Eisenberger, P.; Blumberg, W. E. Observation and Interpretation of X-Ray Absorption Edges in Iron Compounds and Proteins. *Proc. Natl. Acad. Sci. U. S. A.* **1976**, *73*, 1384−1388.
(45) Dey, A.; Jiang, Y.; Ortiz de Montellano, P.; Hodgson, K. O.; Hedman, B.; Solomon, E. I. S K-edge XAS and DFT Calculations on Cytochrome P450: Covalent and Ionic Contributions to the Cysteine-Fe Bond and Their Contribution to Reactivity. *J. Am. Chem. Soc.* **2009**, *131*, 7869−7878.
(46) Mosselmans, J. F. W.; Pattrick, R. A. D.; van der Laan, G.; Charnock, J. M.; Vaughan, D. J.; Henderson, C. M. B.; Garner, C. D. X-Ray Absorption near-Edge Spectra of Transition Metal Disulfides FeS2 (Pyrite and Marcasite), CoS_2, NiS_2 and CuS_2, and Their Isomorphs FeAsS and CoAsS. *Phys. Chem. Minerals* **1995**, *22*, 311−317.

https://doi.org/10.1021/acs.chemmater.4c00490
Chem. Mater. 2024, 36, 6454−6463